Rev. Roum. Sci. Techn.– Électrotechn. et Énerg.
Vol. **71**, *3*, pp. 397–402, Bucarest, 2026

FERRORESONANCE AND SATURATION EFFECTS IN TRANSFORMERS: A FIELD-CIRCUIT APPROACH

ANDREI-DARIUS DELIU[1], EMIL CAZACU [1], FLORENȚIU DELIU[2], CIPRIAN POPA[2]

Keywords: Ferroresonance; Finite element analysis (FEA); Coupled field circuit simulation; Magnetic saturation; Poincaré map; Transformer; Nonlinear dynamics; Jump resonance; Subharmonic ferroresonance; Period-3 oscillation.

The paper presents a time-domain analysis of ferroresonance in a single-phase transformer using a coupled field-circuit model implemented in a finite element method software. The model incorporates the nonlinear magnetic core and an equivalent external circuit including grading and system shunt capacitances. After breaker pole opening, the transformer exhibits stable period-three subharmonic ferroresonance, identified through three-cycle repetition of the induced-voltage and flux-linkage waveforms. Multiple loops in the voltage–flux-linkage phase plane and three clusters in the Poincaré map further confirm this behavior. The dominant flux-linkage component shifts to a period-three subharmonic frequency while its maximum remains unchanged, significantly reducing the peak induced voltage. Thus, the response appears to be subharmonic distortion rather than overvoltage and may not be detected by amplitude-based protection devices. A quantitative existence criterion is derived to define the ferroresonant capacitance range and quantify the damping required to suppress the period-three ferroresonant mode.

1. INTRODUCTION

Ferroresonance is a nonlinear oscillation phenomenon that may occur in electrical power systems when a nonlinear magnetic component (usually the magnetizing inductance of a transformer) is present in the circuit, together with the system capacitances, under certain conditions [1–3]. This phenomenon, unlike linear resonance, can produce sustained overvoltages or overcurrents that can destroy connected equipment [4–6].

The magnetizing inductance of a transformer is highly dependent on its saturation level, and hence small changes in operating conditions can result in abrupt changes in the steady-state behavior [7–11]. Depending on the parameters, ferroresonance can exhibit fundamental, subharmonic, quasiperiodic, or chaotic behavior [12–15]. Ferroresonant modes are investigated using spectral analysis, phase-plane plots, and other techniques [16-18]; mitigation is usually achieved by modifying circuit parameters to avoid the ferroresonant region or by increasing the system's damping [19]. An accurate model of ferroresonance is especially important when hysteresis and nonlinear effects are significant [20-23]. In his study, ferroresonance is explored in a single-phase, no-load transformer using coupled field-circuit simulations [24-28].

The novelty of this paper lies not in creating a new lumped ferroresonance circuit, since these have long been known, but in combining them with a non-linear field-circuit model to achieve three results that matter in practice:

- Replication and classification of a period-three (subharmonic) mode, instead of the fundamental mode that is normally observed.
- A reason for the accompanying drop in voltage, namely the presence of a subharmonic component of the flux, which indicates that a ferroresonant regime does not necessarily imply an overvoltage.
- A rule for selecting the capacitor and the damper.

2. FERRORESONANCE COMPUTATION

Classical ferroresonance models in a transformer-capacitor system assume a series *RLC* circuit with a non-linear inductance. The non-linear magnetizing branch of a transformer core can, under certain switching or initial conditions, generate ferroresonance [3–5].

2.1 CIRCUIT GOVERNING EQUATIONS IN STATE-SPACE FORM

With $v(t)$ the node voltage across the parallel combination of L_m, $C_{parallel}$ and $R_{damping}$ in Fig. 1, the series-capacitor current is:

$$i_s(t) = C_1 \frac{\mathrm{d}}{\mathrm{d}t}\big(v_s(t) - v(t)\big), \tag{1}$$

with C_1 the grading capacitance, $v_s(t)$ the supply voltage source of internal resistance R_1. Both R_1 and the series resistor R_s are initially considered negligible.

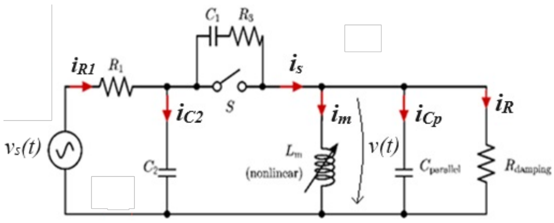

Fig. 1 – Electrical equivalent circuit.

The following notations are used in Fig. 1, primarily to describe the adopted ferroresonant circuit model: i_{C2} denotes the current through the shunt capacitance C_2, i_m denotes the magnetizing current of the nonlinear inductance L_m, i_{Cp} represents the current through the parallel-connected capacitor $C_{parallel}$, and i_R denotes the current through the damping resistor $R_{damping}$.

Kirchhoff's current law at the node gives:

$$i_s(t) = i_m(t) + C_{parallel}\frac{\mathrm{d}v(t)}{\mathrm{d}t} + \frac{v(t)}{R_{damping}}. \tag{2}$$

The magnetizing branch is described through the flux linkage λ, with Faraday's law in lumped form:

$$v(t) = \frac{\mathrm{d}\lambda(t)}{\mathrm{d}t}. \tag{3}$$

The nonlinearity enters through $i_m = g(\lambda)$ [6,7]; the two-state formulation in v and λ is:

$$\begin{aligned} &C_{\text{series}}\frac{\mathrm{d}}{\mathrm{d}t}[v_s(t) - v(t)] = \\ &= g(\lambda) + C_{\text{parallel}}\frac{\mathrm{d}v(t)}{\mathrm{d}t} + \frac{v(t)}{R_{\text{damping}}}. \end{aligned} \tag{4}$$

This system is integrated in time with the switching and initial conditions used in transient runs [28].

[1] Faculty of Electrical Engineering, National University of Science and Technology Politehnica Bucharest, Romania.
[2] Marine Engineering Faculty, "Mircea cel Bătrân" Naval Academy, Romania.
E-mails: andrei_darius.deliu@stud.electro.upb.ro (Correspondence address), emil.cazacu@upb.ro florentiu.deliu@anmb.ro, ciprian.popa@anmb.ro

DOI: 10.59277/RRST-EE.2026.3.10

Figure 2 shows the magnetic equivalent circuit, where Φ denotes the flux passing through the transformer core, while Φ_{parallel} and Φ_{damp} denote the corresponding magnetic fluxes through the parallel $\Re_{\text{paralell}}$ and damping $\Re_{\text{damping}}$ reluctances, respectively.

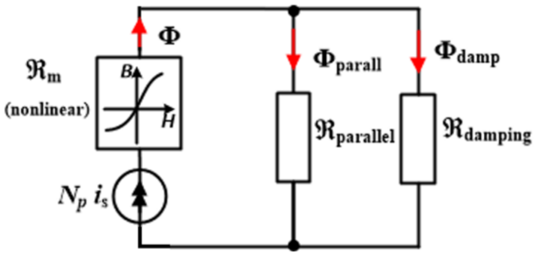

Fig. 2 – Magnetic equivalent circuit.

2.2 THE MATHEMATICAL MODEL

In this study, we use the electromagnetic field model for solid and stranded conductors and the flux linkage as implemented by [22, 28]:

$$\nabla \times (\nu(\mathbf{B})\nabla \times \mathbf{A}) + \sigma\left(\frac{\partial \mathbf{A}}{\partial t} + \nabla V\right) = 0, \tag{5}$$

$$\nabla \cdot \left[\sigma\left(\frac{\partial \mathbf{A}}{\partial t} + \nabla V\right)\right] = 0. \tag{6}$$

Here, **B** is the magnetic flux density, **A** is the magnetic vector potential, V is the electric potential, ν is the magnetic (nonlinear) reluctivity, and σ is the electric conductivity.

In nonconducting regions, the second term in (5) vanishes; in conducting parts, it captures eddy currents. The Coulomb gauge ensures the uniqueness of the magnetic vector potential, while a reference value and appropriate interface conditions are prescribed for the magnetic scalar potential. The computational domain is sufficiently large to account for the decay of the leakage field outside the transformer.

This model is used mostly for low-frequency simulations, so the radiation term is ignored. First-order edge elements for the magnetic vector potential and second-order nodal elements for the electric potential are used. The *tree-cotree* method provides uniqueness of the magnetic vector potential **A**. The degrees of freedom of edge elements on the spanning tree of the finite element mesh are set to zero. This formulation is used throughout the computational domain, except for stranded conductors.

2.3 FERROMAGNETIC CONSTITUTIVE LAW

In the core region, the key nonlinearity is introduced through the measured/tabulated *B–H* curve, so that local saturation directly affects the flux distribution, the magnetizing current, and the induced voltages. The coil/circuit coupling relates terminal voltage to flux linkage:

$$\lambda(t) = N_p\Phi(t) \;= N_p\int_S \mathbf{B}(t)\cdot \mathrm{d}\mathbf{S}, \tag{7}$$

where N_p denotes the number of turns of the primary winding, to which $v(t)$ and $\lambda(t)$ are referred throughout this study. The quantity $\Phi(t)$ denotes the magnetic flux crossing the core cross-section S and linking one turn, whereas $\lambda(t)$ denotes the total primary-winding flux linkage; the hat notation, as in $\hat{\Phi}$ or $\hat{\lambda}$, is reserved for peak values.

2.4 TRANSFORMER, CORE MATERIAL AND NETWORK PARAMETERS

A single-phase 1 kVA, three-limb transformer of rated voltages 230 V / 24 V (AC) is investigated here, with primary N_p = 300 and secondary N_s = 32 turns (ratio a = 9.375). The three-limb core has a stepped limb. Its dimensions and rated data are indicated in Table 1. The secondary is modeled under open-circuit (no-load) conditions via a very large load resistance, as in experimental ferroresonance test configurations [3]. For the applied supply voltage, the peak flux linkage is imposed by Faraday's law: $\hat{\lambda} = \sqrt{2}\cdot U_I/\omega$ = 1.035 Wb, hence $\hat{\Phi} = \hat{\lambda}/N_p$ = 3.45 mWb. Here, U_1 represents the rated primary voltage value, and ω is the angular frequency at 50 Hz. With the net limb section $A_c \approx 5.7\cdot10^{-3}$ m², the section-averaged peak flux density at nominal voltage is $\hat{B}_{av} \approx 0.61$ T.

Table 1

Transformer parameters

Parameter	*Value*
Topology	Single-phase, 3-limb core
Rated voltages	230V / 24V AC
Rated Power	1 kVA
Primary Turns	300
Secondary Turns	32
Limb cross-section "outer diameter" d	90 mm
Limb center-to-center distance	160 mm
Yoke center-to-center distance	250 mm
Rated primary current I_{1N}	4.35 A
Net limb cross-section A_c	≈ $5.7\cdot10^{-3}$ m²
Peak flux linkage $\hat{\lambda} = \sqrt{2}\cdot U_1/\omega$	1.035 Wb

Our numerical model is adapted from the ANSYS model library and has a homogeneous core (no laminations) and block windings symmetrically positioned on the middle column, as shown in Fig. 3.

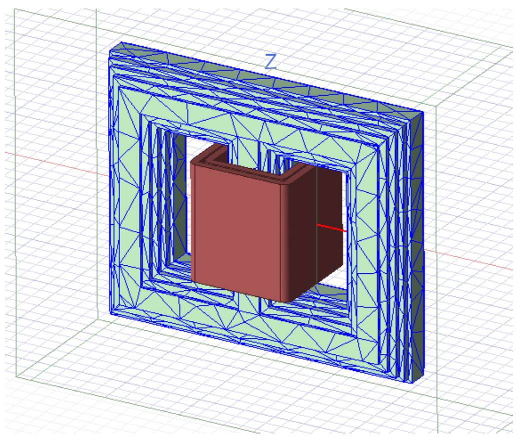

Fig. 3 – 3D Mesh Plot of the three-limb transformer.

The supply terminals of the windings are shown in Fig. 4. In the field-circuit coupling, each winding is driven through a terminal, a cross-section sheet of the winding volume on which the external circuit imposes the winding current. The four sheets in Fig. 4 map one-to-one onto the primary and secondary pins of the transformer block.

For numerical computational reasons, the domain is limited by an open boundary condition introduced in subsection 2.2. This numerical model, correlated with the magnetic circuit of Fig. 2, is only notional; the main goal of our study is to illustrate ferroresonance and saturation effects. The core material is M400-50A non-oriented electrical steel, represented by the tabulated *B–H* curve of Fig. 5. The effect of the material non-linearity is modeled by a single-valued characteristic, *i.e.*, saturation without hysteresis [8], as is usually done for ferroresonance modeling [6].

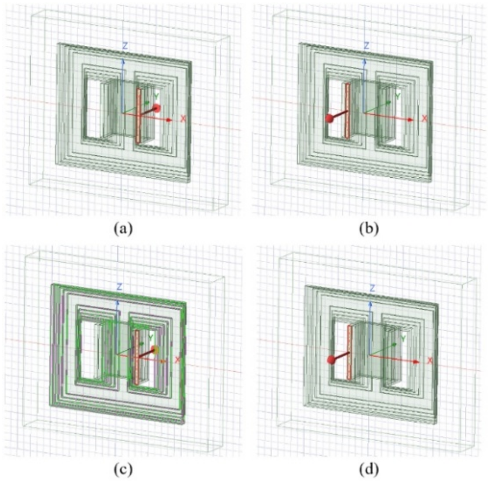

Fig. 4 – Winding supply terminals of the field-circuit model: (a) primary in; (b) primary out; (c) secondary in; (d) secondary out. The red sheet is the terminal cross-section of the winding.

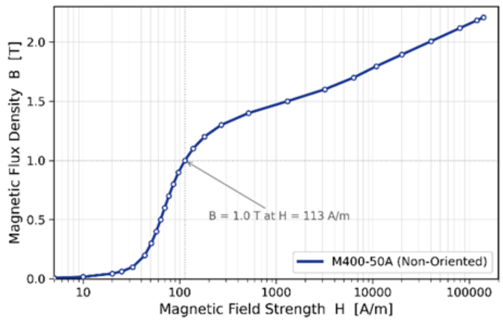

Fig. 5 – Magnetic characteristic of M400-50A material.

The model was meshed using 17,707 tetrahedra, 4,029 of which were in the core. With an RMS core edge length of 51.4 mm compared to a 90 mm limb width, the limb cross-section contains less than two elements per side. This is sufficient to resolve the integral quantities that couple the field to the circuit ($\lambda(t)$ is calculated as the surface integral of B, and then $v(t)$ follows from it), but not the local flux density distribution because each first-order tetrahedral element stores only one value of B.

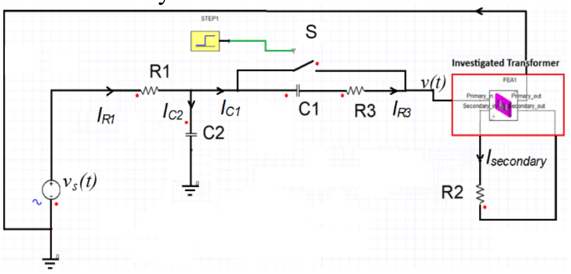

Fig. 6 – External circuit.

The external network, illustrated in Fig. 6, represents the breaker-grading and system shunt capacitances [9], including a grading (equalizing) capacitor C_1 in series with a grading resistor R_3 connected, a standard element in single-phase ferroresonance equivalents [4–10]. On the source side of S, a shunt (phase-to-ground) capacitance C_1=13 μF is included. A source series resistance R_1=0.020 Ω represents source damping, while the open-circuit secondary condition is enforced by a very large resistance R_2 =10^{12} Ω.

The parameter values in Table 2 complete the set needed to simulate the nonlinear magnetic element and the capacitive network required to excite ferroresonance [11,19,24,25]. R_1 is the only external element. This value represents the supply internal resistance: the transformer winding resistances are accounted for by the finite-element model of the coil, arising from the physical properties of the conductor material and geometry, and should not be considered part of the external circuit.

Table 2

Circuit model parameters

Parameter	*Value*
Grading capacitance (across phase-A contact) C_1	1.2 μF
Grading series resistor R_3	1.5 Ω
Shunt capacitance (phase-to-ground) C_2	13 μF
Load resistance (open-circuit emulation) R_2	$1 \cdot 10^{12}$ Ω
Source series resistance R_1	0.020 Ω
Supply effective voltage E_1	230 V, 50 Hz
Opening instant of S	0.165 s

The switching sequence is as follows. From t = 0, S is closed, the grading branch is short-circuited, and the transformer is energized directly through R_1; this interval contains the energization (inrush) transient. At t = 0.165 s, S opens, inserting C_1–R_3 in series between the source and the primary and leaving the unloaded saturable magnetizing branch in series with a capacitance; this is the standard representation of a breaker pole that has interrupted the current while its grading capacitor remains connected.

Note that C_2 lies on the source side of S, across the source and its 0.020 Ω resistance: since R_1/X_{C2} = $8 \cdot 10^{-5}$, C_2 is effectively short-circuited and does not participate.

2.5 SELECTION OF THE EXTERNAL-CIRCUIT PARAMETERS AND EXISTENCE CONDITION

After S opens, the source is in series with the grading circuit and the non-linear magnetizing branch. If we ignore resistances, we have $U_1 = \mathrm{j}(X_L - X_C)I$ and $U_L = \mathrm{j}X_L I$, and therefore the working points are found at the intersections between the magnetization curve $U_L(I)$ and the capacitor load lines $U_L = \pm U_1 + X_C I$. Three intersection loops, thus also the jumping and the possibility of a permanent regime, are possible only when the slope of the load line (given the magnetic properties of the core) falls between those of the saturated and non-saturated parts of the curve [5,7,13],

$$\omega L_{sat} < \frac{1}{\omega C_{series}} < \omega L_m, i.e.,$$

$$\frac{1}{\omega^2 L_m} < C_{series} < \frac{1}{\omega^2 L_{sat}}. \qquad (8)$$

For $L_m = N_p{}^2 \mu_0 \mu_r A_c / l_{\mathrm{eff}}$, $l_{\mathrm{eff}} = 0.535$ m being the effective length of the two parallel flux loops of this core, and $\mu_r \approx 7 \cdot 10^3$ at $\hat{B}_{av}$≃0.61 T, we get L_m≃8 H, X_L ≃2.6 kΩ beyond the knee, the differential permeability goes down to a few hundred, yielding X_{sat}≃10^2Ω.

Inequality (8) shows that the ferroresonant window lies between 1 μF and a few tens of μF. The 1.2 μF in Table 2 is close to the lower bound, at $C_{cr} = 1/(\omega^2 L_m)$, or the minimum capacitance for which the load line intersects the characteristic three times. This value was obtained from bound (8) and adjusted in trial simulations until a sustained oscillation occurred upon opening S. Below C_{cr}, the region of multiple solutions vanishes, and the transformer settles back in its normal no-load operating condition; above the upper bound, the loop remains inductive at any excitation level. The grading resistance determines $Q = X_L/(R_1 + R_3 + R_w) \approx 10^3$, making the loop essentially undamped. Forcing $Q < 10$ would require more than 2·10² Ω in series, which is incompatible with the purpose of a grading resistor. Thus, series damping does not work in this case, and damping must be applied across the magnetizing branch. A load resistance R_b on the 24 V secondary appears on the primary side as a^2R_b with $a^2 = (300/32)^2 = 87.9$. Demanding $a^2R_b \lesssim X_L$ leads to $R_b \lesssim 30\ \Omega$, which amounts to approximately 20 W or 2 % of the rated power.

3. SIMULATION RESULTS

The proposed ferroresonance model was simulated using [28] for 1.0 s. The following subsection analyzes and interprets the results in terms of the ferroresonance phenomenon.

3.1 TIME-DOMAIN ANALYSIS AND JUMP RESONANCE

Figure 7 depicts the time-dependent variation of the induced primary voltage (Fig. 7a), primary current (Fig. 7b), and flux linkage (Fig. 7c). At $t = 0$, the switch S closes and opens at the instant $t_{sw} = 0.165$ s (after the inrush current vanishes).

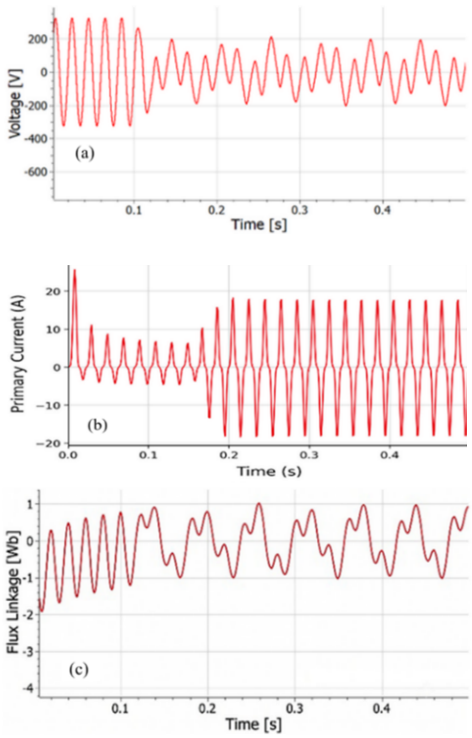

Fig. 7 – (a) Induced primary voltage, (b) primary current and (c) flux linkage, versus time.

The induced voltage (Fig. 7a) and the flux linkage (Fig. 7c) change together, being coupled through the relation: $v = d\lambda/dt$. Before t_{sw}, the voltage is sinusoidal, with a peak value of 325 V ($\sqrt{2}U_1$), while $\hat{\lambda}$=1.035 Wb.

Immediately afterward, both become non-sinusoidal; the voltage peak drops to approximately 216 V, while $\hat{\lambda}$ remains at 1.04 Wb. Fig. 7b shows the current changing at about 0.16 s, corresponding to the same instant. The current depends on λ via $i = g(\lambda)$. It is almost flat below the knee, so while the change in $\lambda(t)$ shape at the peak alters the waveform, the peaks change little.

During the first interval, the current envelope is controlled by the decay of the transient energization: the initial value in Fig. 7c is -1.91 Wb, with an offset that decays with a time constant of around 35 ms. The steady state is not a fundamental-frequency oscillation. The voltage peaks repeat every 20 ms in Fig. 7a, but their magnitudes repeat only every three power cycles: 200, 122, and 78 V from $t = 0.384\ s$ to 0.425 s; these values are repeated 60.3 ms later as 197, 132, and 88 V. The extrema in Fig. 7c repeat every two alternating intervals of 43.4 and 17.0 ms, for a total of 60.4 ms, with two maxima per period.

The result is a subharmonic response of order three, with fundamental frequency $f_s/3 = 16.67$ Hz, and a dominant flux-linkage component at $2f_s/3 = 33.3$ Hz. This also accounts for the lower voltage. As $\hat{v} = \omega_d\hat{\lambda}$, and since $\hat{\lambda}$ did not change and ω_d is now $2\omega/3$, the anticipated peak value would be $(2/3)\cdot 325 = 217$ V, compared to 216 V. The flux linkage curve (Fig. 7c) is like the voltage curve. Its peak value is 1.035 Wb before and 1.04 Wb after the switching, equal to $\sqrt{2}U_1/\omega$; the transition modifies the frequency components of $\lambda(t)$, not its amplitude.

3.2 PHASE-PLANE ANALYSIS AND POINCARÉ MAP

To describe the period of oscillation, the path is drawn in the phase plane (flux linkage vs. induced voltage).

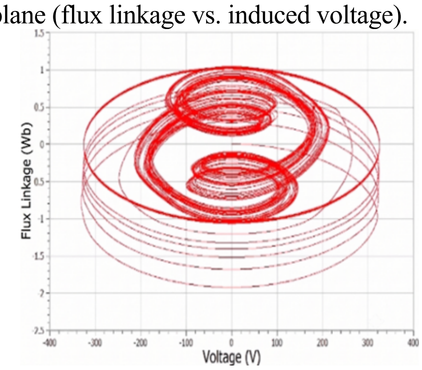

Fig. 8 – Phase–plane representation.

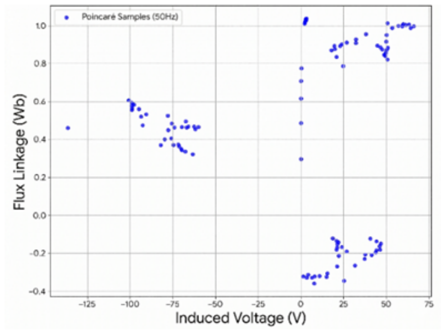

Fig. 9 – Poincaré map, sampled at 50 Hz.

As seen in Fig. 8, the path contracts from the large excursions of the energization transient and converges to a bounded attractor which is not a single closed curve but rather a set of interlaced loops. The fact that these loops are interlaced already suggests that the period is a multiple of the supply period. To find out that multiple, the state (λ, v) is sampled stroboscopically at $T = 20$ ms as in Fig. 9 (the Poincaré map).

Together with the phase plane, the Poincaré map shows:

- Transient phase: the trailing string of points at $v \approx 0$, with λ from 0.29 to 1.03 Wb, traces the migration towards the attractor.
- Steady state: the samples do not converge to a single point but accumulate in three well-separated clusters, near (−75 V, +0.45 Wb), (+45 V, +0.92 Wb) and (+30 V, −0.25 Wb).

Three clusters in a map sampled at the supply period mean that the state repeats only after three supply periods: the regime is a subharmonic ferroresonance of order three, $T = 3T_s = 60$ ms, of fundamental $f_s/3 = 16.67$ Hz. This agrees with the 60.3 and 60.4 ms periods of subsection 3.1, so three independent indicators from the same solution give the same classification.

3.3 CORE SATURATION AND FIELD DISTRIBUTION

We compute the transient regime using the magnetoquasistatic *A-V* formulation of Section 2.2 and the tabulated *B-H* curve [7, 22] with edge elements, implicit backward-Euler time integration, and a Newton iteration on the tangent permeability [26]. This iteration tolerance, combined with the mesh density, determines the accuracy of the local field values presented below.

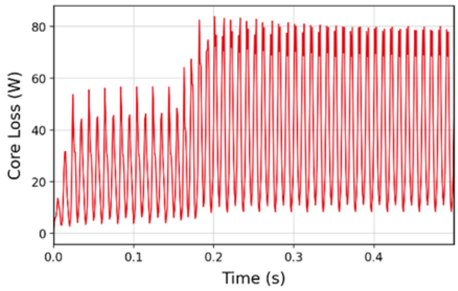

Fig. 10 – Core loss during ferroresonance.

Figure 10 displays the instantaneous core loss over the same interval; the pulses increase from peak values of about 55 W to approximately 80 W, indicating additional thermal stress and accelerated insulation aging associated with extended operation [12, 16]. This record is not synchronized with Fig. 7a and 7c, and the lamination is not resolved, so the values are indicative and cannot be compared directly with the measured no-load loss.

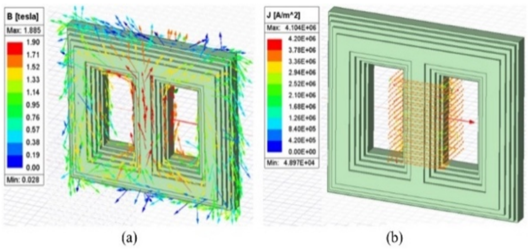

Fig. 11 – (a) Flux density vectors and (b) current density vectors in the primary winding, during ferroresonance.

Figure 11a shows a vector plot of the flux lines. The vectors are all contained within the iron path, and the calculated peak values reach about 1.89 T, compared to the section-averaged nominal value of 0.61 T, *i.e.*, in the saturated region of the M400-50A magnetization curve (Fig. 5).

Fig. 11b presents the instantaneous current density vectors J in the primary winding during a ferroresonant peak.

As the core enters the strongly magnetized state, the differential inductance of the magnetizing branch falls, creating a temporarily low-impedance path for the source and the concentrated current density of Fig. 11b, whose computed maximum is of the order of $4\cdot10^6$ A/m².

These concentrations correspond to the sharp current peaks, indicating electrodynamic and thermal stress on the winding during the ferroresonant regime.

4. DISCUSSION

These observations lead us to draw four additional conclusions (which do not merely reiterate that resonance arises from a capacitive-inductive interaction).

- This regime is a third-order subharmonic, as evidenced by three distinct criteria, but in this case the terminal voltage decreases rather than increases; therefore, it cannot be detected by amplitude-based protection and requires a frequency-based criterion (*e.g.*, the presence of a component at $f_s/3$) or a stroboscopic one.
- The criterion imposed by (8) confines the phenomenon to a capacitance window bounded below by $1/(\omega^2 L_m)$ and above by $1/(\omega^2 L_{sat})$ here about 1 μF to a few tens of microfarads, giving the design rule that the equivalent series capacitance seen by an unloaded transformer must stay below $C_{cr} = 1/(\omega^2 L_m)$, with L_m available from the routine no-load test.
- Only the capacitance between the open contact and the terminal of the transformer counts, since the upstream capacitance in shunt is short-circuited by the source; the summation of all capacitances present on the busbars would be highly nonconservative and would here give an error of the order of 11.
- Mitigation must be applied to the magnetizing branch: about 30 Ω and 20 W on the secondary are sufficient, while damping in series is useless.

The field solution provides insight into the device's inner workings: the flux is entirely confined within the iron, the core operates in the nonlinear region of the hysteresis curve, and the winding current density is concentrated during the saturation pulses. These features give rise to forces proportional to $\mathbf{J} \times \mathbf{B}$ and to an instantaneous increase in core loss [13, 15, 17, 18]. On the other hand, the terminal behavior can be described quantitatively: the maximum value of the flux linkage remains 1.035 Wb (value determined by the source) before and after the occurrence of the ferroresonant phenomenon; furthermore, the energy of the system is concentrated at $f_s/3$ and $2f_s/3$.

In field applications, the phenomenon is facilitated by the presence of an unloaded or lightly loaded transformer, a poorly damped circuit, and an equivalent capacitance between the disconnecting switch and the transformer terminals, all within the interval defined by (8). Solutions to this problem are keeping the equivalent series capacitance below C_{cr}, loading the secondary with a resistance $R_b \leq 30\ \Omega$, and using controlled switching when an unloaded transformer needs to be energized in the presence of a grading capacitance.

4.1 LIMITATIONS

The limitations of the model and methodology adopted for this study are as follows:

- The use of a single-valued *B-H* curve does not account for remanence, coercivity, or minor loops; thus, switching effects are not included in the simulation.
- The effect of lamination in the magnetic core is neglected.
- The model is larger than typical commercial transformers, and although its qualitative behavior is similar, it is not fully representative.
- No experiments were conducted to validate the model.

A summary of the numerical results is listed in Table 3.

Table 3

Summary of the main numerical results.

Quantity	Observed value / behaviour	Engineering meaning
Ferroresonant transition	Initiated at 0.165 s; established within ≈ 0.1 s	Opening of S inserts the grading capacitance
Maximum flux density	≈ 1.89 T	
Poincaré map	Three distinct clusters	Subharmonic ferroresonance of order three, $T = 3T_s = 60$ ms
Peak flux linkage	1.035 Wb before / 1.04 Wb after	Unchanged; fixed by $\sqrt{2}\cdot U_1/\omega$
Induced-voltage peak	325 V → 216 V	Ratio 2/3: signature of the $2f_s/3$ component

The findings of this research paper indicate that further work, involving additional simulation studies and possible physical testing, should be carried out to extend this analysis.

5. CONCLUSION

We have shown here the combined field-circuit simulation of ferroresonance in a single-phase transformer, using an M400-50A core and an external network that includes the grading and shunt capacitances that are present in actual installations. For the data in Tables 1 and 2, the model replicates a stable ferroresonant condition that starts when the switch is opened at $t = 0.165\ s$ and stabilizes after a transient of about 0.1 s. It is a subharmonic ferroresonance of order three with period $T = 3T_s = 60$ ms, as evidenced by the three-fold repetition of the induced-voltage and flux-linkage waveforms, by the three loops of the phase plane plot, and by the three clusters of the Poincaré section.

The maximum flux-linkage value remains constant before and after the onset, 1.035 Wb compared to 1.04 Wb, but the main frequency of the flux linkage changes to $2f_s/3$, so the maximum induced voltage drops from 325 V to 216 V, a reduction by 2/3, as expected for a third-order subharmonic. The phenomenon is therefore a waveform-distortion mode rather than an overvoltage one and would not be detected by an amplitude threshold.

The analysis provides insight into the design parameters: the grading capacitance is situated at the critical boundary defined by the inequality $1/(\omega^2 L_m) < C_{series} < 1/(\omega^2 L_{sat})$; only the capacitance on the load side of the switch is active; and a resistive load of around 30 Ω dampens the resonance, but a series resistance does not.

The present work identifies several areas for further improvement. A mesh-convergence and solver-refinement study, together with the synchronous export of all transient quantities, are therefore identified as the immediate next steps.

CREDIT AUTHORSHIP CONTRIBUTION

ANDREI-DARIUS DELIU: conceptualization, formal analysis, numerical simulations, methodology, data curation, validation, visualization, writing (draft, review, and editing).
EMIL CAZACU: conceptualization, investigation, validation, supervision, writing (review and editing).
FLORENȚIU DELIU: investigation, numerical simulation, writing (draft), methodology.
CIPRIAN POPA: formal analysis, investigation, numerical analyses, and computation.

ACKNOWLEDGMENT

This work was supported by a doctoral scholarship awarded to the PhD student author, Andrei-Darius Deliu, by the National University of Science and Technology POLITEHNICA Bucharest.

REFERENCES

1. M. Nagpal, Z. Jiao, S.H. Manuel, T. Martinich, S. Merriman, D. Sydor, "Sub-synchronous ferroresonance causes catastrophic failure of a line shunt reactor – a postmortem investigation," IEEE Trans. Power Deliv., **37**, *1*, pp. 374–382 (2022).
2. S. Singh, R. Yadav, A.K. Pradhan, "Phasor-based identification of CVT ferroresonance with divergent density distribution of intrinsic modes," IEEE Trans. on Industry Applications, **61**, *2*, pp. 2835–2845 (2025).
3. S.J. Kruger, J.A. de Kock, "Ferroresonance: a review of the phenomenon and its effects," Southern African Universities Power Engineering Conference/Robotics and Mechatronics/Pattern Recognition Association of South Africa (SAUPEC/RobMech/PRASA), pp. 1–6 (2021).
4. V. Simha, W.-J. Lee, "The jump phenomena," IEEE Industry Applications Magazine, **14**, *5*, pp. 53–59 (2008).
5. P. Ferracci, *Ferroresonance*, Schneider Electric, Cahier technique no. 199 (2001).
6. S. Jazebi, A. Farazmand, B.P. Murali, F. de Leon, "A comparative study on PI and T equivalent models for the analysis of transformer ferroresonance," IEEE Trans. on Power Deliv., **28**, *1*, pp. 526–528 (2013).
7. M.R. Iravani et al., "Modeling and analysis guidelines for slow transients – Part III: the study of ferroresonance," IEEE Trans. Power Deliv., **15**, *1*, pp. 255–265 (2000).
8. B. Lakshmi Praba, R. Seyezhai, "Flicker-free resonant DC-DC SEPIC converter with valley-fill for LED applications," Rev. Roum. des Sci. Tech. Ser. Electrotech. Energ., **70**, *1*, pp. 47–52 (2025).
9. E. Cazacu, L. Petrescu, "Qualitative and quantitative aspects of the ferroresonance phenomenon in low-voltage electrical installations (in Romanian)," Electrical Machines, Materials and Drives – Present and Trends, **16**, *1*, pp. 76–92 (2020).
10. E. Cazacu, L. Petrescu, "Power quality issues generated by the nonlinear resonance occurrence in electric networks," International Conference and Exposition on Electrical and Power Engineering (EPE), pp. 023–026 (2022).
11. J. Wiśniewski, E. Anderson, J. Karolak, "Susceptibility of electrical network to ferroresonance occurrence," Computer Applications in Electrical Engineering, **8**, pp. 46–52 (2010).
12. E. Cazacu, L. Petrescu, V. Ioniță, "Ferroresonance analysis of particular iron core transformers," 12th International Symposium on Advanced Topics in Electrical Engineering (ATEE), Bucharest, Romania, pp. 1–6 (2021).
13. D.A.N. Jacobson, P.W. Lehn, R.W. Menzies, "Stability domain calculations of period-1 ferroresonance in a nonlinear resonant circuit," **17**, *3*, pp. 865–871 (2002).
14. B.A. Mork, D.L. Stuehm, "Application of nonlinear dynamics and chaos to ferroresonance in distribution systems," IEEE Trans. Power Deliv., **9**, *2*, pp. 1009–1017 (1994).
15. M. Zou et al., "Nonlinear dynamic analysis of periodic ferroresonance based on a novel hysteresis approach," Modern Physics Letters B, **30**, *9*, 1650164 (2016).
16. M. Mikhak-Beyranvand et al., "Impacts of ferroresonance and inrush current forces on transformer windings," IET Electric Power Applications, **13**, *7*, pp. 914–921 (2019).
17. J.A. Corea-Araujo et al., "Tools for characterization and assessment of ferroresonance using 3-D bifurcation diagrams," IEEE Trans. on Power Delivery, **29**, *6*, pp. 2543–2551 (2014).
18. F. Wörnle, D.K. Harrison, C. Zhou, "Analysis of a ferroresonant circuit using bifurcation theory and continuation techniques," IEEE Trans. on Power Delivery, **20**, *1*, pp. 191–196 (2005).
19. I.G.N.S. Hernanda, I.M.Y. Negara, D.A. Asfani, D. Fahmi, N.I. Rifma, M. Wahyudi, "Experiment based on analysis of series and shunt capacitance to ferroresonance response on low voltage transformer," 4th IEEE Conf. Power Eng. Renew. Energy, ICPERE, pp. 1–6 (2018).
20. D. Chouaibi, W. Chagra, "A new hybrid optimization method used in predictive control of a nonlinear fractional model based on fractional Hammerstein structure," Rev. Roum. des Sci. Tech. Ser. Electrotech. Energ., **69**, *4*, pp. 437–442 (2024).
21. P.S. Moses, M.A.S. Masoum, H.A. Toliyat, "Dynamic modeling of three-phase asymmetric power transformers with magnetic hysteresis: no-load and inrush conditions," IEEE Trans. Energy Convers., **25**, *4*, pp. 1040–1047 (2010).
22. S. Vujevic, "A new look at Maxwell's equations and wave equations in conducting media," 32nd Int. Conf. Software, Telecommun. Comput. Networks, SoftCOM, pp. 1–7 (2024).
23. J.C. Lacerda Ribas, E.M. Lourenco, J.V. Leite, N.J. Batistela, "Modeling ferroresonance phenomena with a flux-current Jiles–Atherton hysteresis approach," IEEE Trans. Magn., **49**, *5*, pp. 1797–1800 (2013).
24. V. Torres-García, N. Solís-Ramos, N. González-Cabrera, E. Hernández-Mayoral, D. Guillen, "Ferroresonance modeling and analysis in underground distribution feeders," IEEE Open Access Journal of Power and Energy, **10**, pp. 583–592 (2023).
25. S. Boutora, H. Bentarzi, "Study of ferroresonance favorable cases in electric substations," Rev. Roum. des Sci. Tech. Ser. Electrotech. Energ., **63**, *4*, pp. 359–364 (2018).
26. A. Tokic, J. Smajic, "Modeling and simulations of ferroresonance by using BDF/NDF numerical methods," IEEE Trans. Power Deliv., **30**, *1*, pp. 342–350 (2015).
27. V. Stefanescu, F.I. Hathazi, G. Rată, C. Ungureanu, "Technical losses caused by poor power quality in electrical networks with nonlinear consumers," Rev. Roum. des Sci. Tech. Ser. Electrotech. Energ., **70**, *3*, pp. 337–342 (2025).
28. ***https://ansyshelp.ansys.com/public/Views/Secured/Electronics/v242/en/Subsystems/Maxwell/Content/APhiFormulationinMaxwell3DTransient.htm(accessed 01.07.2026).